Insight on the optoelectronics and enhanced dielectric properties of strontium decorated PbI_2 nanosheets for hot carrier solar cell applications

S. Muthu Mariappan, Mohd. Shkir, T. Alshahrani, V. Elangovan, H. Algarni, S. AlFaify

PII: S0925-8388(20)34126-8

DOI: https://doi.org/10.1016/j.jallcom.2020.157762

Reference: JALCOM 157762

To appear in: *Journal of Alloys and Compounds*

Received Date: 4 July 2020

Revised Date: 9 September 2020

Accepted Date: 28 October 2020

Please cite this article as: S.M. Mariappan, M. Shkir, T. Alshahrani, V Elangovan, H. Algarni, S. AlFaify, Insight on the optoelectronics and enhanced dielectric properties of strontium decorated PbI_2 nanosheets for hot carrier solar cell applications, *Journal of Alloys and Compounds*, https://doi.org/10.1016/j.jallcom.2020.157762.

CRediT authorship contribution statement

All authors contributed equally in all sections of the article.

Insight on the optoelectronics and enhanced dielectric properties of strontium decorated PbI_2 nanosheets for hot carrier solar cell applications

S. Muthu Mariappan[1], Mohd. Shkir*[2], T. Alshahrani[3], Vinoth Elangovan[4], H. Algarni[2], S. AlFaify**[2]

[1]*Department of Physics, Vel Tech Multitech Dr. Rangarajan Dr. Sakunthala Engineering College, Chennai-600 062, Tamilnadu, India.*

[2]*Advanced Functional Materials & Optoelectronics Laboratory, Department of Physics, College of Science, King Khalid University, Abha 61413, Saudi Arabia.*

[3]*Department of Physics, College of Science, Princess Nourah Bint Abdulrahman University, Riyadh, 11671 Saudi Arabia.*

[4]*Functional Materials and Energy device Laboratory, SRM Institute of Science and Technology, Kattankulathur, Chennai, Tamilnadu, India.*

*Corresponding author

E-mail: shkirphysics@kku.edu.sa

Abstract

Dielectric properties determine by electric field distributions play a decisive role in energy harvesting and storage applications. In this context, strontium decorated lead iodide nanosheets (Sr:PbI_2) are prepared, and its vibrational and dielectric properties are studied. The bandgap changes are explained by Brustein-Moss effect and renormalization process. Raman spectral studies reveal that introducing Sr atoms into PbI_2 lattice enhance the lifetime of LO phonon through bottleneck effect. Subsequently, the dielectric constant (ε′) values of 5 wt.% Sr:PbI_2 are increased 20% than pure PbI_2. The results conclude that the vibrational properties of Sr decorated PbI_2 nanosheets are much significant for hot carrier solar cell devices.

Keywords: *Lead iodide (PbI_2); optoelectronics; Burstein-Moss effect; dielectrics; electrical properties.*

1. Introduction

Fascinating properties of various oxide and nitride based wide bandgap semiconductors are being studied predominantly over past few decades. Validating this, an improved trend in device performances of such semiconducting materials can be observed from plenty of reports [1–7]. On the other hand, interest shown on halide-based semiconductors is comparatively low and most of their properties are yet to be discovered. Among different halide-based semiconductors, lead iodide (PBI_2) is a noteworthy material due to its technological viability for various applications. Indeed, PbI_2 is a layered compound with alternative stacked I-Pb-I layers arranged sequentially along vertical axis (i.e. *z*-axis) [8]. Resembling graphite structure, atoms in same layers of PbI_2 are strongly glued together with covalent bonding and nearby layers atoms are weakly hold by Van der Waals force [9]. Precise control on PbI_2 number of layers by heat treatment process and the corresponding changes in absorption bands were examined by Goto et al. [10]. Insight on radiative

mechanism of PbI_2 have confirmed the existence of both bi-excitonic and exciton-exciton collisions, which makes their emission properties quiet interesting [11]. Ando et al. demonstrated that, bottleneck effect in PbI_2 provides missing link between its anomalous emission properties and optical phonons [12]. The observed bottleneck effect in PbI_2 are much essential to improve the performance of lead halide based perovskite solar cells [13]. Confirming this, very recently the decisive role of PbI_2 on the actions of perovskite solar cells was revealed by Gujar et al. [14]. Yet, a profound analysis on the absorption properties of PbI_2 are much needed to effectively use them in optoelectronic devices like photodetectors and photovoltaics, etc. Besides, their dielectric properties are also much reliable for energy storage applications [15].

Owing to its quasi two dimensional (2D) anisotropic layered structure, PbI_2 can be easily modified into novel morphologies such as thin nanowires, nanorods, and nanosheets, etc [16, 17]. Though 1D materials disclose important properties like high surface to volume ratio, its electronic properties are dubious with predominant noise arising through carrier trapping at defect sites, also defect free nanowires generally require expensive preparation technique [18, 19]. But dielectric applications require a smooth, high density, and low conducting material with large surface area. Hence, 2D-PbI_2 nanosheets with larger bandgap and reasonable dielectric constant (ε') are ideal candidates for such applications.

In earlier days, considerable amount of research works on PBI_2 have focussed its nuclear radiation detection properties due to high stability of lead against nuclear reactions and its strong electron density [20, 21]. But in contemporary days, profound knowledge on engineering materials with cutting edge tools and available state of the art characterization techniques have turned out to be a driving factor for researchers to unravel its nano-regime properties. Modification in intrinsic semiconductors like (i) doping foreign atoms at different lattice sites (or at interstitial position), (ii) making composites with suitable compounds, and

(ii) tuning its morphology to provide high surface to volume ratio could results in interesting properties [22, 23]. Various reports have demonstrated the importance of dopant elements in both n-type and p-type semiconductors. For example, in oxide-based semiconductors, presence of oxygen defects play a positive role in photocatalysis via inducing redox reaction. However, same defects act as a recombination site for excitonic carrier and degrade the performance of photovoltaic devices. Hence, depending upon application purpose, defects should be tuned with suitable dopant atoms at optimum composition. Similarly, halide semiconductors with different dopants can provide improved performance with enriched properties. Our previous works on noble metal nanoparticles decorated PbI_2 sheets exhibits improved photo-detecting performance by virtue of surface plasmon resonance (SPR) of metallic nanoparticles in near infrared region [24]. Also, we examined optoelectronic and improved dielectric properties of neodymium (lanthanide group) doped PbI_2 nanorods [25]. However, to the best of our facts there is no exclusive report to monitor the optical, phonon, and dielectric properties of alkaline metal decorated PbI_2 nanosheets. To fill this void, we prepared strontium decorated PbI_2 nanosheets (Sr:PbI_2) with microwave assisted technique and analysed its structural and optoelectronic properties for hot carrier solar cells. In the final section, the impact of Sr atoms on the dielectric properties of PbI_2 are studied.

2. Experimental procedures

Fabrication and investigational details

For the preparation of pure PbI_2 and Sr:PbI_2 samples, we initially procured high grade lead acetate (LA), sodium iodide (NaI), strontium nitrate (SN), cetyl trimethylammonium bromide (CTAB), and acetic acid (AA) from Sigma and Alfa Aesar Pvt. Ltd. Com. In the first step, solutions of 0.5M LA and 1M NaI were dissolved separately in 50 ml of DDW at 60 ºC and respective solutions were named A and B. Followed by that, 50 ml of CTAB solution from a stock of CTAB (30g/1000 ml) was added to A, and stirred for 15 min. Then, 50 ml of

AA was added to same solution to catalyst the reaction. Next, solution B was poured into solution A under same temperature and stirring conditions. Subsequently, a yellow colour precipitate appears while pouring first drop of NaI itself, clearly indicates the formation of aimed PbI_2. Later, the solution was collected in cylindrical flask and placed in indigenously modified microwave system of 700 W power and irradiated for 15 min. Finally, the solution was cool down to room temperature and the precipitate was collected after washing with DDW several times. Finally, the precipitate is dried at 80 ºC in an oven for 24 h. Similar process is followed to prepare Sr:PbI_2 samples with additional solution of 1 wt.%, 3 wt.% and 5 wt.% of SN into the LA solution. The synthesis procedure is represented in Fig.1.

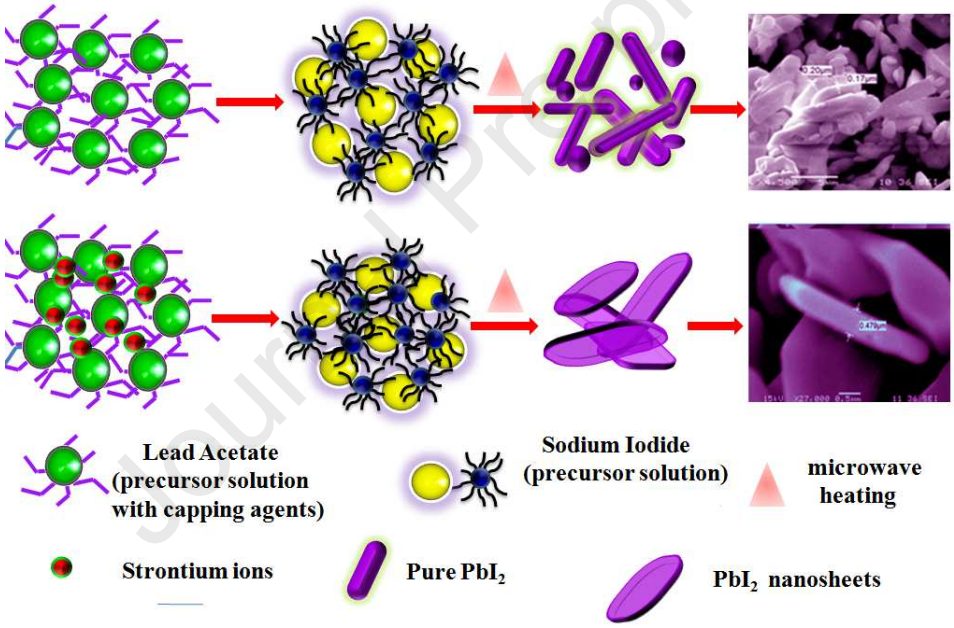

Fig. 1: Schematic of the synthesis procedure and the formation of pure PbI_2 and Sr:PbI_2 samples

All these prepared samples were inspected by Lab X6000 XRD system for phase identifications [$CuK_{\alpha 1}$, λ=1.54056 Å; operating conditions- 40kV/30A; scan rate - 2 º/min; scan range - 5 to 70º]. Additionally, Rietveld refinement process was carried out through MAUD version 2.33 of Rietveld [L. Lutterotti: program Maud (version 2.33), city)] and real-time refinement of structure was done by a least-squares refinement progression. Optical

absorption analysis performed with JASCO V570 system was used to analyse the impact of Sr atoms on the band structure of PbI_2. The surface morphology, elemental composition and homogeneity in final products were recorded by JEOL JSM6360 SEM/EDX system. For vibrational modes identifications, a high-precision DXR FT-Raman setup with 532 nm laser operated at 0.2 mW power was used. The dielectric properties were measured from 4200-SC setup and prior to measurements all samples were converted into a pellet of dimensions 10 mm diameter and 0.70 mm of thickness by applying 5 ton of pressure with a pelletizer.

3. Outcomes and discussion

3.1. Phase identification

Structural properties of all samples are inspected from XRD profiles. As shown in Fig. 2(a), peaks obtained for pure PbI_2 and Sr:PbI_2 are exactly matching with its standard diffraction values [JCPDS 7-0235]. The lack of additional phases and well defined sharp peaks decline the presence of impurities during growth process and the same results are further confirmed with EDX/Raman measurements.

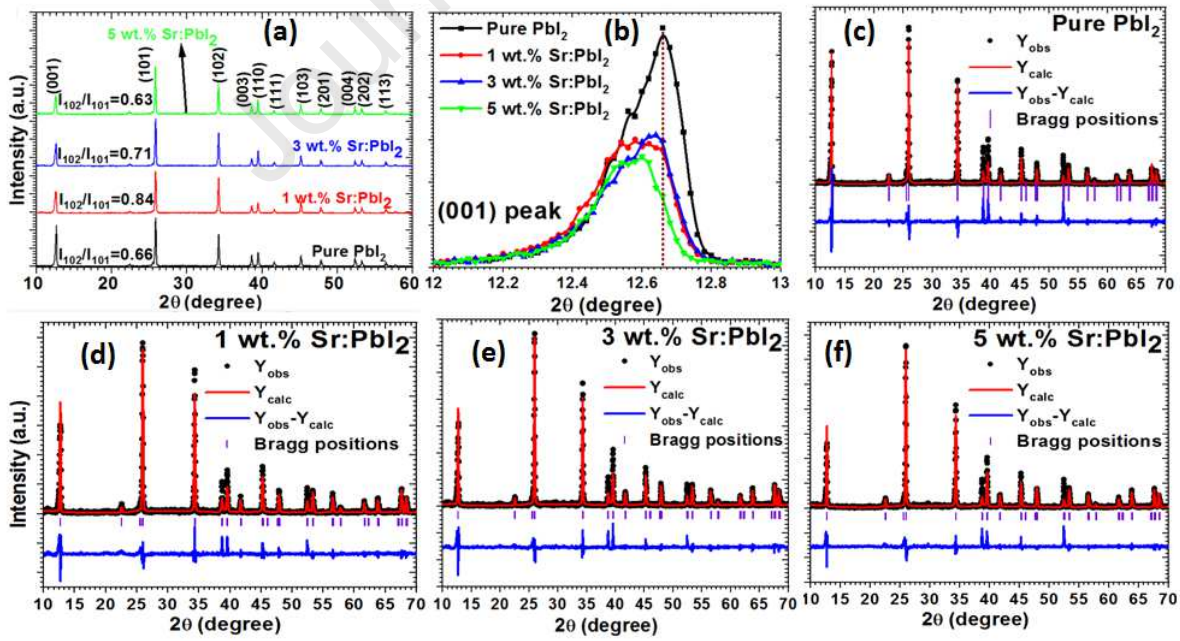

Fig. 2: (a) XRD pattern of pure PbI_2 and Sr:PbI_2. (b) Magnified view of (001) peak. (c-f) Rietveld refinement data for pure PbI_2 and Sr:PbI_2.

PbI_2 is an iso-structural material with over 50 different polytypes have been displayed so far, and the corresponding space groups are determined by number of symmetry elements exist in the structure [26]. Majority (i.e. > 95%) of PbI_2 compound possess a smaller number of symmetry element and leads to the formation of 2H-*P3m1* space group as reported in this article. The term 2H represent that Pb layers are stacked between two hexagonal honeycombs shaped I layers with different stacking orientation as shown in Fig. 4.

Further, changes in crystallite size (D) of prepared samples are calculated by Scherrer formula: $D = \frac{0.9\lambda}{\beta\, cos\theta}$, where $\lambda,\ \theta,\ \beta$ represent the wavelength of the Cu-K_α radiation (1.5406Å), diffraction angle and the full width half maximum (FWHM), one-to-one. As shown in table 1, the crystallite size is found to decrease with increasing Sr wt.%, whereas the lattice constants increases. Such phenomenon is termed as *size-induced negative pressure effect*. It's a commonly occurring process in covalent semiconductors to maintain the symmetry to a long range. Such observation has been previously reported in other transition semiconductors like Fe_2O_3, CuO and CeO systems [26].

Also, the lattice constants a, c are calculated by standard equations through POWDERX software, see Table 1. The ratio between c/a are approximately 1.53, which exactly matches with the previously reported value [27]. The similar dopant dependent variations in the structural parameters are also confirmed by Rietveld refinement process [Fig. 2 (c-f)]. The error in the refinement parameters are minimized to about ± 0.001 Å by carefully performing the experiments and repeated refinements.

Table 1: Calculated structural parameters for all samples from POWDERX software and Rietveld refinement processes.

Sample	POWDERX software			Rietveld refinement parameters			D	δ_{101} $\times 10^{-4}$	ε_{101} $\times 10^{-3}$
$Pb_{1-x}Sr_xI_2$	*a* (Å)	*c* (Å)	V (Å^3)	*a* (Å)	*c* (Å)	V (Å^3)	(nm)	(nm^{-2})	
x=0.0 wt. %	4.55636	6.97999	125.49349	4.5556	6.9756	125.3754	56.276	3.158	2.757
x= 1.0 wt. %	4.55628	6.98211	125.52738	4.5548	6.9766	125.3460	47.658	4.403	3.257
x= 3.0 wt. %	4.55711	6.98233	125.57702	4.5555	6.9773	125.3951	52.038	3.693	2.982
x= 5.0 wt. %	4.55892	6.98294	125.68798	4.5550	6.9765	125.3554	52.913	3.572	2.935

The influence of dopant atoms on preferential growth direction of PbI_2 is monitored from intensities of different diffraction peaks. Although there are no significant changes has been observed in intensities of most of the peaks, there is a slight increase can be noticed in (102) plane of the 1 wt.% and 3 wt.% Sr:PbI_2 samples. In addition, there is a considerable amount of reduction has been observed in the intensities of (001) plane of all Sr:PbI_2, along with a small shift towards lower diffraction angle. This decrement in the (001) plane intensity suggest that, growth of nanorods are highly restricted with the presence of Sr dopants and the same fact has been confirmed from SEM image. Typically, the lower angle shifts in the XRD peaks are mainly attributed to the biaxial tensile stress induced inside the PbI_2 lattice due to the dopant atoms (see Fig. 2(b)) [28]. These observations imply that the ratio of dopant to the parent concentration plays a fair role on the preferential growth directions. As the experimental conditions for all samples are similar, the dopant atoms introduced into PbI_2 structure should be the only reason for inducing stress and influence the growth directions. The increased lattice parameter consequently increases the values of calculated unit cell volume (see Table 1). Insight on the broadening of (001) plane and increased intensity in (102) plane is done by calculating the lattice strain (ε) and dislocation density (δ) with

respective formulas; $\varepsilon = \frac{\beta \times \cot\theta}{4}$ and $\delta = \frac{1}{D^2}$, where β and θ corresponds to the FWHM and the corresponding diffraction angle respectively. The calculated values of ε and δ are given in Table 1. It can be observed that dopant atom causes an increased ε and δ values. Vegard's law suggests that variations in the unit cell dimensions are linked to ionic radii of dopant atom and provide a pathway to reveal the exact location of dopant atom. As the ionic radii of Sr^{2+} are almost equal to Pb^{2+} ions, it can be speculated that increase in unit volume is due to the replacement of Sr atoms with the Pb atoms. But it is not possible due to the strong electronegativity values of Pb^{2+} (2.33) compared to Sr^{2+} (1.00). Therefore, the increments in the unit cell dimensions are only due to the interstitial occupancy of Sr atoms and caused the observed stress.

3.2. Optical absorption spectrum analysis

Modifications in band structure of PbI_2 with interstitial Sr atoms could be ascertained by optical absorption spectra. The recorded absorption spectra are shown in Fig. S1 (see supplementary information). For precise calculation of band gap (E_g) we adopted Tauc's plot approach instead of energy-wavelength relation ($E_g = \frac{hc}{\lambda}$). Since PbI_2 is a direct bandgap semiconductor, E_g values are measured by extrapolating linear section of $(\alpha h\nu)^2$ curve to intersect the horizontal axis of $h\nu$ vs $(\alpha h\nu)^2$ graph, where α is absorption coefficient of PbI_2 and $h\nu$ is the energy of incident photon. The intersecting point of extrapolating line on $h\nu$ axis (i.e. $(\alpha h\nu)^2 = 0$) gives accurate band gap. For calculation purpose, the value of α is obtained by Beer- lamberts law; $\alpha = 2.303A/d$ where A is absorbance value and d is path length (i.e. thickness of the cuvette, 10 mm). As shown in Fig. 3, bandgap of pure PbI_2, 1 wt.%, 3 wt.% and 5 wt.% Sr:PbI_2 are calculated as 3.26 eV, 3.29 eV, 3.28 eV, and 3.26 eV respectively. Zhang et al. reported that, bandgap of PbI_2 will decrease with the increasing concentration of iodine concentration when PbI_2 is sandwiched between two perovskite

layers. The decrease may be attributed to the cationic exchange/ interactions between PbI_2 and the perovskites [29]. However in our case, compared to pure PbI_2, widening of E_g of about 0.03 eV is observed in 1wt.% Sr:PbI_2, and followed by a narrowing down of E_g occurs for 3 wt.% and 5 wt.% Sr:PbI_2.

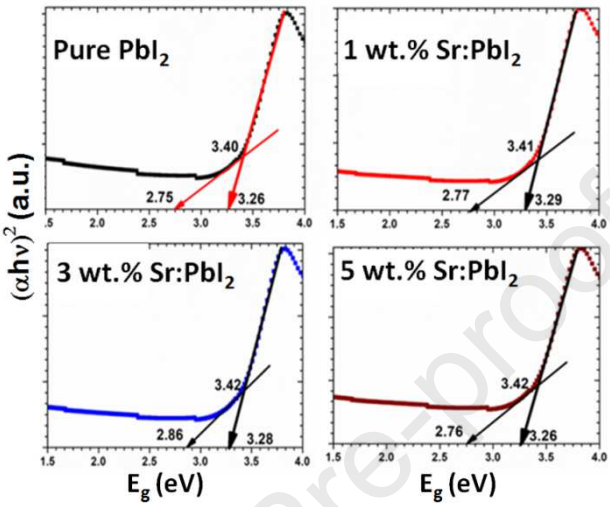

Fig. 3: Tauc's plots for pure PbI_2 and Sr:PbI_2, corresponding bandgap values are marked.

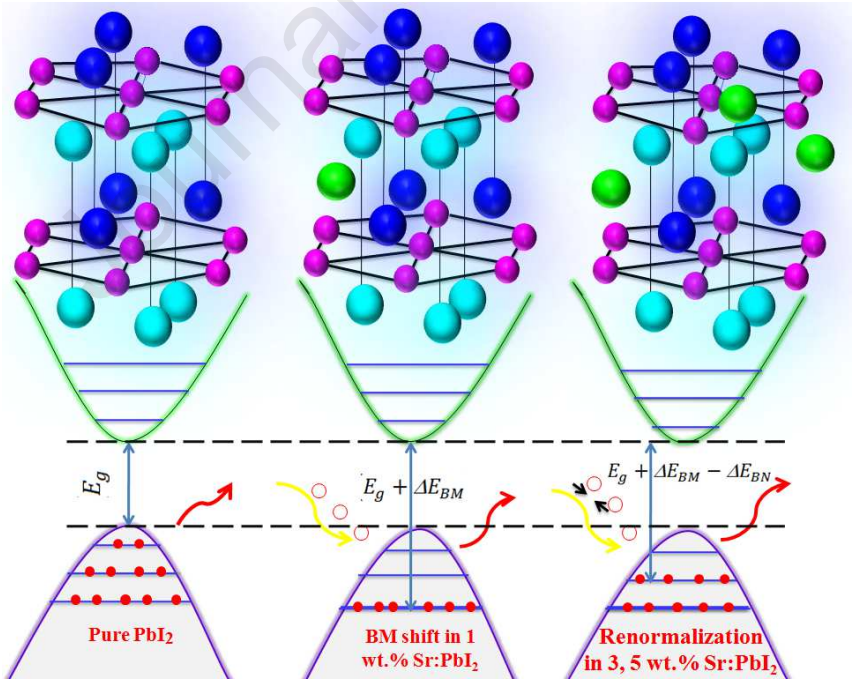

Fig. 4: Schematic representation of bandgap widening and narrowing by Burstein-Moss mechanism and renormalization process. (Iodine - dark blue and cyan blue, Pb- pink, Sr- green).

The band gap widening is commonly attributed to different mechanisms such as (i) Burstein-Moss (BM) shift, (ii) quantum confinement effect, or (iii) excitation dependent absorption widening, etc. [30, 31]. But the mechanism (ii) and (iii) will be effective only when particle size is curtailed to the Bohr radius diameter and the surface to volume ratio of the samples are very high. Therefore, those mechanisms can be deliberately excluded as no such 0D or 1D morphology is observed from SEM image. Hence the only pathway for widening of E_g can be the Burstein-Moss (BM) shift. Though widening in E_g by BM shift has been reported in surplus of n-type of materials, to the best our knowledge this is one of the infant observations in a direct p-type material. However, to understand the increase in E_g of p-type material by BM shift mechanism, it is significant to recall the same mechanism in n-type material [32]. With the Fermi level near to conduction band edge, carrier concentration of n-type semiconductors will be increased with electron donor dopant atoms. Owing to filled density of states near the conduction band edge, Fermi level will shift into conduction band with an upward transition of ΔE_{BM} (Brustein Moss shift). Consequently, absorption takes places between the top of valence band edge to the Fermi level inside conduction band. Hence, band gap is apparently increased to $(E_g + \Delta E_{BM})$ rather than the actual band gap (E_g). On the other hand, introducing hole dopants like Sr into PbI_2 (p-type semiconductors), where Fermi level located near the valence band edge, the added holes recombine with the electrons near the upper electronic states of valence band [33]. Thus, the Fermi level makes a downward transition and leads to an increased band gap as shown in Fig 4. Therefore, with the addition of 1 wt.% Sr dopant, it increases the band gap of PbI_2 by injecting holes into the parent semiconductor. However, with the higher concentration of Sr dopant atoms, the band gap shrinks due to a renormalization process which generally results from phenomena like (i) carrier-carrier thermalization, (ii) carrier- ionic impurity interactions, and (iii) carrier- optical phonon interactions etc. Such renormalization process downshift the

bottom edge of conduction band and reduce the bandgap of the sample [34, 35]. Theoretical modelling of such shift has been reported by Zhu et al. in pure CdO films [35]. But due to the difficulties in developing such unequivocal theory to connect E_g values of PbI_2 with Sr wt.%, we analysed the bandgap variations by numerical methods. The E_g values correspond to different Sr concentrations are obtained by cubic spline plot analysis (see supplementary Fig. S2), and it is clear that the E_g values starts to decrease at 1.58 wt.% of Sr dopant. In addition, linear curve fit methods show that observed variation in E_g can be related with the supplementary equation 1 (see supporting data).

3.3. Morphological and EDX analysis

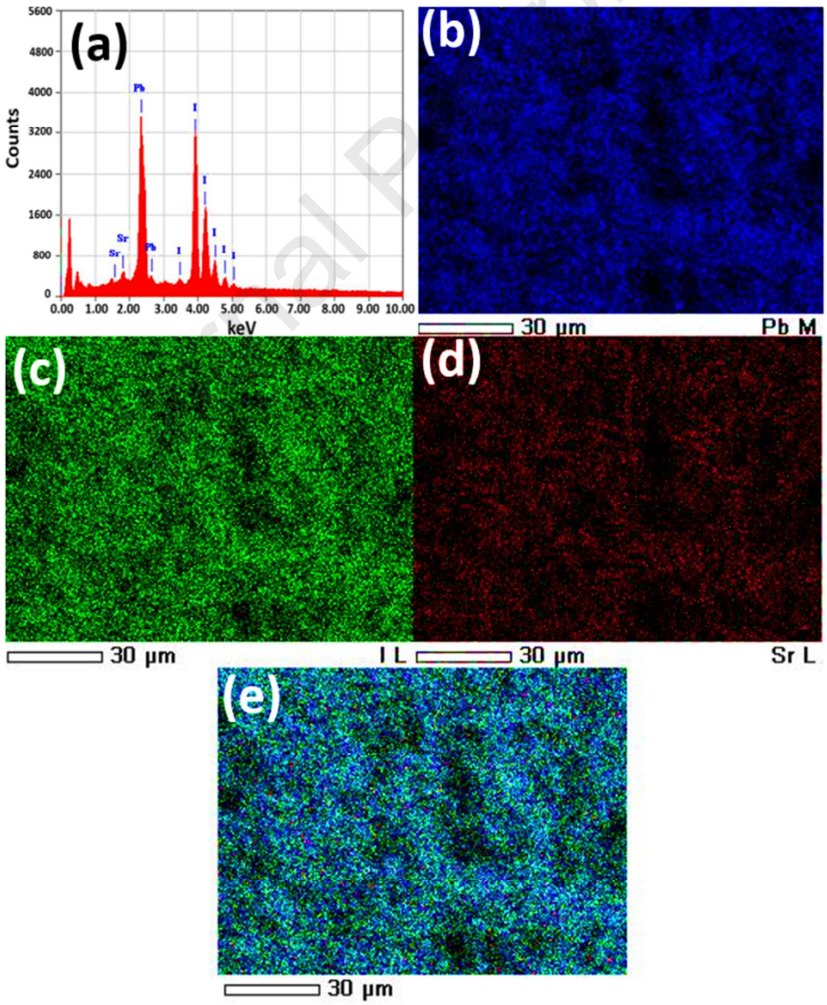

Fig. 5: (a) EDX profile (b-e) SEM-mapping images for Pb (blue), I (green), Sr (red) and the overlay of Pb, I, Sr for 3.0 wt.% Sr:PbI_2.

Elemental compositional analysis and morphological imaging were performed with EDX/SEM elemental mapping (e-mapping) and SEM imaging, respectively. The peaks in EDX spectra [Fig. 5(a)], confirm the presence of Pb, I, and low weight percentage of Sr atoms respectively. Further, SEM e-mapping endorse the homogenous distribution of crystallites without any agglomerations, even in 3 wt.% Sr:PbI_2 [Fig.5 (b-e)]. Then, surface morphologies of pure PbI_2 and Sr:PbI_2 are recorded with different SEM resolutions (see Fig. 6).

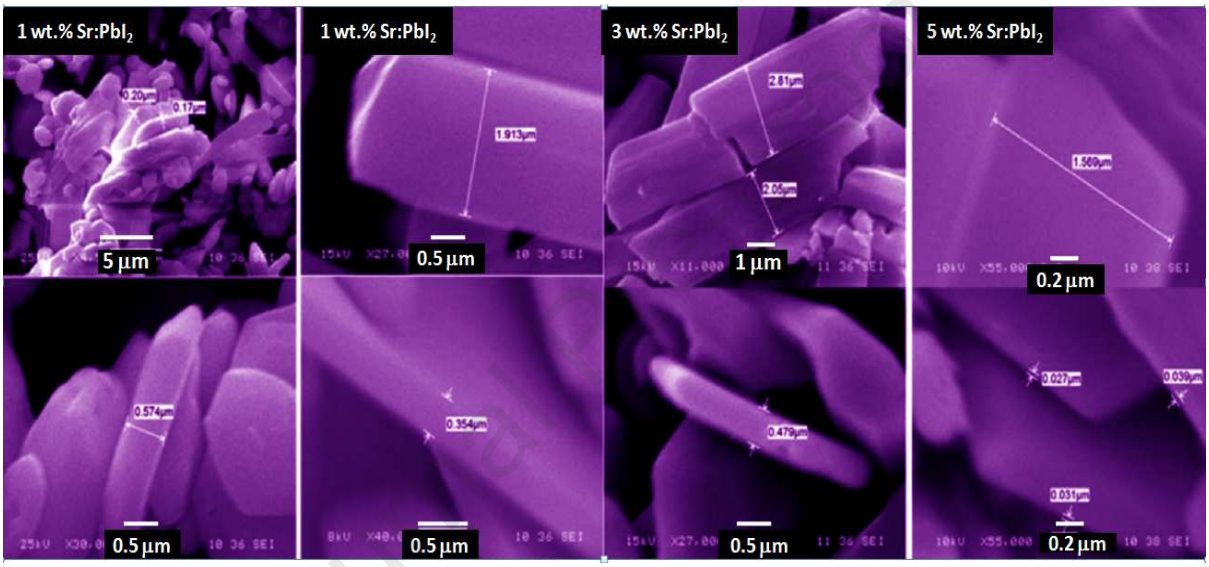

Fig. 6: SEM micrographs of pure PbI_2 and Sr:PbI_2. The corresponding sheet thickness variations are shown below in the respective samples.

It can be observed that, pure PbI_2 consists of mixed spherical nanoparticles with few protruding nanorods of thickness 0.17 µm and width 0.574 µm, which indicates that particles tend to grow along *c*-axis for given experimental conditions. However, morphology of 1 wt.% Sr:PbI_2 spreads into two dimensional (2D) nanosheets of width 1.913 µm and thickness of 0.354 µm. This observation implies, growth along *c*-axis is highly restricted in 1 wt.% Sr:PbI_2 and similar observation is evidenced from XRD analysis. The same trend has been observed with increase in Sr dopant concentration and to understand such morphological

changes, a possible growth process is much needed from the formation of PbI_2 seed layers as provided by following equation,

$$Pb(CH_3COO)_2 + 2NaI \rightarrow PbI_2 + 2NaCH_3COO.$$

The cationic exchange model suggests that formed nanocrystals tend to elongate into 1D nanorods with the presence of surfactant like CTAB. Though various parameters can influence preferential growth direction such as temperature, nature of surfactant, and pH values of the reaction media, the resultant PbI_2 nanosheets are quite surprising because of the similar experimental conditions for all samples. Hence, the big picture of such observation is that, "dopant Sr atom must be the cause for the change in morphologies of Sr:PbI_2". In general, planes normal to preferred growth direction possess minimum surface area and eventually sample morphologies are determined by the available formation energy along each direction. Hence a time resolved growth mechanism with the presence of Sr atoms is necessary to unfold the evolution process. To start with, the formation energy of pure PbI_2 along c-axis must be initially higher to kinetically favoured its growth along (001) plane. However, with the addition of Sr atoms 1D nanorods experience high reactivity at the ridges which is the main reason for the spreading of nanosheets [36, 37]. Moreover, as evidenced from XRD analysis, incorporating Sr atoms into PbI_2 will create defects along (001) plane which further decreases the formation energy along (001) plane and facilitates growth along different direction other than c-axis. Thus, in a binary step growth process, growth along c-axis is initially hindered and then favours the growth along (102) plane to achieve a thin nanosheets. Such observation has been noticed previously in the Fe doped ZnO lattice [38].

3.4. Vibrational analysis:

Raman spectroscopy is a significant characterization to analyse the number of layers in 2D structured materials. The relative intensity changes, frequency shift, and broadening in Raman bands could provide information about phonon lifetime and carrier-phonon

interactions in the semiconductor. The recorded Raman spectra are shown in supplementary Fig. S3 (see supporting information) and in-order to extensively analyse the system, we de-convolute the bands and presented in Fig. 7. As the unit cell in 2H-PbI_2 consists of 3 atoms, the possible 3N vibrational modes are represented by 6 irreducible phonon modes: $\Gamma = A_{1g} + 2A_{2u} + 2E_u + E_g$. Hence, the peaks obtained at 73 cm^{-1}, 93 cm^{-1}, 110 cm^{-1}, 167 cm^{-1}, and 216 cm^{-1} corresponds to E_u(TO), A_{2u}(TO), A_{2u}(LO), and the overtone modes, respectively. Yagmurcukardes et al. has reported the position of A_{2u}(TO) mode, for different layer of PbI_2 [39]. According to their report, our nanosheet should possess less than 5 layers. The vibrational properties of absorbent layer play a crucial role in determining the performance of perovskite hot carrier solar cells. Especially the phonon bottleneck effect arising as a result of weak carrier-phonon interaction facilitates the confinement of incident light energy inside the system.

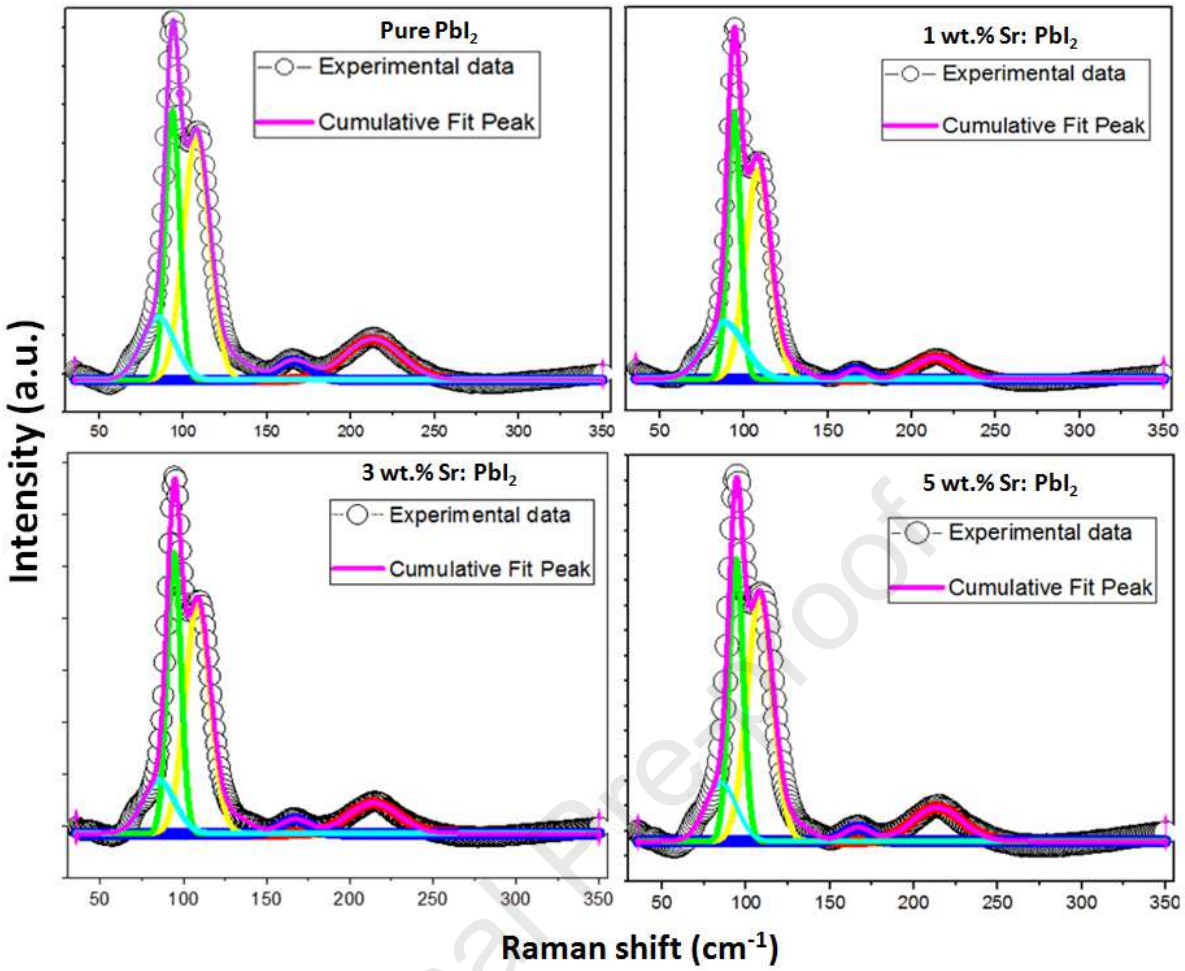

Fig. 7: Fitted Raman data after base line corrections and the de-convoluted peaks are differentiated with different colours.

Table 2: FWHM and Phonon lifetime of A_{2u} (TO) and A_{2u} (LO) modes

Samples	A_{2u} (TO)			A_{2u} (LO)		
	Peak Position (cm^{-1})	FWHM	Phonon life time (ps)	Peak Position (cm^{-1})	FWHM	Phonon life time (ps)
Pure- PbI_2	93.63	8.29	0.6402	107.90	16.74	0.31
1 wt.% Sr- PbI_2	93.96	7.85	0.6761	108.53	15.17	0.35
3 wt.% Sr- PbI_2	94.2	8.32	0.6379	108.63	15.26	0.34
5 wt.% Sr- PbI_2	93.98	8.53	0.6222	108.26	15.41	0.34

Table 2 shows the phonon lifetime (τ) of longitudinal optical phonon $A_{2u}(LO)$ and transverse optical phonon $A_{2u}(TO)$ calculated by the equation: $\frac{1}{\tau} = 2\pi c\Gamma$, where c, Γ are the

velocity of light and the FWHM of corresponding band. The lifetime of $A_{2u}(LO)$ is found to be slightly increased for 1 wt.% Sr:PbI_2. In general, the properties of LO phonon is very significant, because, when the incident light photons create excitons immediately its energy is transferred into LO phonon and finally dissipates as heat via acoustic phonon. However, if the carrier concentration is very high, it forms a bottleneck like structure to escape into LO phonon, consequently the lifetime of excitonic carrier and LO phonon will be increased. Thus, the increased lifetime of $A_{2u}(LO)$ is attributed to bottleneck effect induced by large carrier density inside Sr:PbI_2. Such phonon bottleneck effect in PbI_2 with enormous carrier density has previously confirmed with photoluminescence studies by Ando et al [12]. Contrarily, at higher doping concentration, large carrier-carrier interaction results in renormalization process as discussed in absorption studies. Also, the intensity of the Raman band at $A_{2u}(TO)$ at 96 cm^{-1} is highly enhanced in 1 wt.% Sr:PbI_2 samples due to the improved crystalline quality. A similar observation has been revealed by Baibarac et al. due to the exciton-phonon coupling in PbI_2, yet a lower temperature analysis is required to intuitively study such changes [40]. These observations have revealed that, role of Sr dopant in PbI_2 could play a crucial role on the efficiency of the photovoltaic devices.

3.5. Dielectric studies

Owing to the dependency of charge storage ability on its dielectric properties, its associated parameters such as dielectric constant (ε′), dielectric loss (tan δ), and AC conductivity gains attention as it directly infers about the feasibility of PbI_2 to apply in energy storage devices. The dielectric studies are carried out by metal-insulator-metal (MIM) technique, where samples are initially made into pellets and then sandwiched between Cu electrodes on both sides of pellets. Later, the required bias voltage is applied across metallic electrodes to provide electric field across the sample. In general, ε′ is a complex quantity

where its real part signifies degree of polarization (i.e. stored electrical energy) and imaginary part reveal the dissipated energy.

Fig. 8(a,b) show the values of ε′ and tan δ of pure PbI_2 and Sr:PbI_2 samples over a wide frequency range. All dielectric parameter calculations were performed as from our previous report [25]. A 10% and 20% increase in ε′ has been observed for 3 wt.% and 5 wt.% Sr:PbI_2 samples, meanwhile ε′ values of 1 wt.% Sr:PbI_2 and pure PbI_2 samples are almost overlapping. Except for a small hump at low frequency region, the values of ε′ are almost constant in entire frequency range. The variation trend in ε′ values insists that the dielectric mechanism is same for all sample at a given frequency. The derivative of ε′ values are shown in Fig. 8c. Thus, unravelling reason for increasing values of ε′ at high sr wt.% and small hump at low frequency region are much needed. To understand the dielectric behaviour of sample, insight on the conduction mechanism is crucial which generally involves (i) hopping conduction, (ii) space charge induced conduction, (iii) Poole-Frenkel emission, and (iv) Ohmic conduction [41]. Due to the large bandgap of PbI_2, current could not increase significantly for small bias voltage. Hence the Ohmic conduction might not be the reason for downward trend in ε′ value after the small hump in low frequency region. Similarly, the Poole-Frenkel conduction, often called intrinsic Schottky conduction require high temperature for inducing sufficient carriers; hence it can also be conveniently omitted as all experiments are carried out in room temperature. Hence, the observed hump in low frequency region can be only due to core intrinsic polarization properties and not due to experimental parameters and external conditions. Maxwell-Wagnel model suggest that, lattice is composed of different grain separated by walls/boundaries.

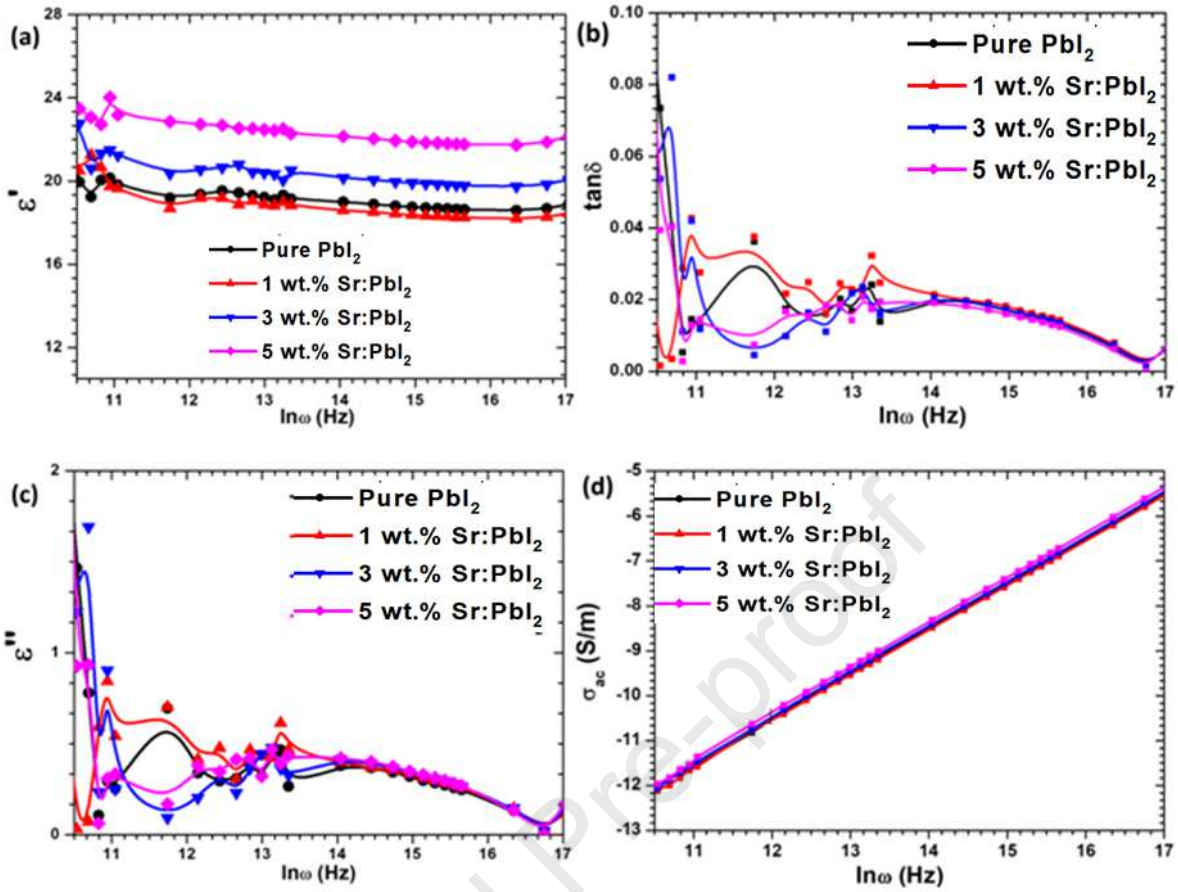

Fig. 8: Plots for (a) ε' vs. ln(ω), (b) $tan\delta$ vs. ln(ω), (c) ε'' vs. ln(ω), (d) σ_{ac} vs. ln(ω) of0 wt.% 1 wt.%, 3 wt.% and 5 wt.% Sr decorated PbI_2 nanosheets.

The carrier can freely move only inside the volume of given grain and cannot percolate into grain boundaries. Thus, a polarization will induce across the grain boundary for an applied electric field. On the other hand, it's a well-established fact that at low frequency region the ε′ and tan δ values are highly dominated by space charge results from commonly observed lattice vacancy and possibly some dangling bonds. Further the hopping carriers trapped inside grain could deteriorate the conduction and results in small hump at low frequency region. Also, the presence of sr atoms at high concentration could possibly increases the existing ionic vacancies. Hence large Sr interstitials significantly improve oriental polarization values due to the difference in electronegativities in Sr^{2+} and Pb^{2+} [42]. Consequently, the ε′ values are increased for 3 wt.% and 5 wt.% Sr:PbI_2. However, in high

frequency region, the ε′ values are almost constant, suggesting that the dipole does not obey the applied field in that region. In fact, large damping of dipoles results in slight downward trend in the ε′ values at higher frequencies. Desirably the dielectric losses are very low in all cases as shown in Fig. 8(b).

Further, the AC conductivity (σ_{AC}) of pure PbI_2 and Sr:PbI_2 samples are calculated and corresponding values are plotted in Fig. 8(d). Irrespective of dopant concentration, all the samples show improved σ_{AC} values at high frequencies. Such increase can be attributed to the enhanced drift mobility of the carrier as a result of hopping conduction [43]. As shown in inset of Fig. 8(d), there is a slight increase in conductivity of 3 wt.% and 5 wt.% Sr:PbI_2 samples. This can be explained by the large number of carriers induced by S interstitial atoms and the obtained results are consistent with the dielectric values. Further, the frequency dependent σ_{AC} conductivity is analyzed by the standard Jonscher's equation: $\sigma_{AC}(\omega) = \sigma_{DC} + A\omega^s$, where σ_{DC} is the DC conductivity (i.e, σ at $\omega_{\to 0}$) and *s*, A are the frequency exponent and a constant respectively. The value of *s* is obtained by fitting the slope of *ln* σ_{AC} *vs ln* ω as reported in our previous work [24, 25]. As shown in supplementary Fig. S4 (see supporting information), *s* value initially increases and then slowly decreased at high Sr wt.%. The average value of *s* is around unity and in general it's a temperature dependent quantity. Hence a detailed work on the temperature dependent analysis of ε′ is required. The schematic diagram shown in Fig.9. illustrates the charge separation phenomena in Sr:PbI_2.

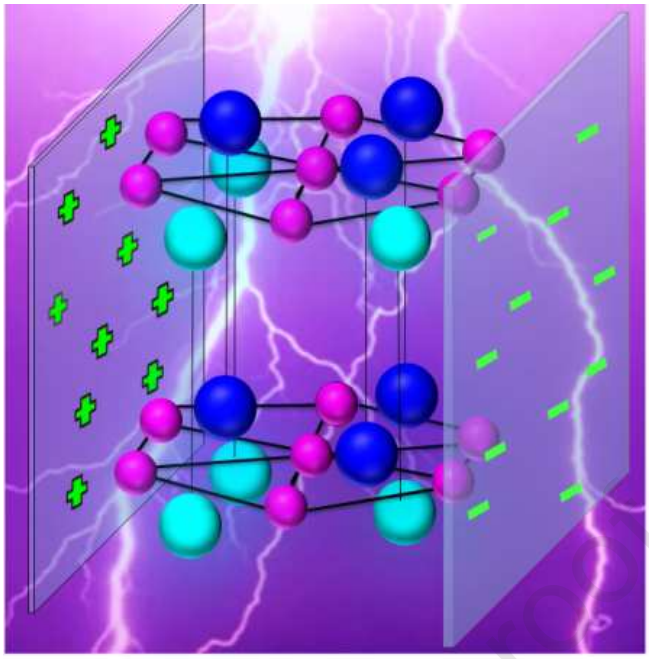

Fig. 9: Schematic representation of charge storage mechanism in PbI_2 nanosheets with applied electric field (shown by lightning).

4. Conclusions:

In summary, Sr:PbI_2 were prepared by microwave assisted synthesis process. XRD analysis suggest that, Sr atoms suppress the tendency of pure PbI_2 to grow along the (001) plane, rather it favours the (102) plane as preferential growth directions. Based on the stress induced on PbI_2 structure by Sr atoms as confirmed by structural analysis, a possible mechanism has furnished for the spreading of nanosheets. Compared to pure PbI_2, the bandgap values are found to be increased of 0.03 eV at 1wt.% Sr:PbI_2, however the trend starts decreasing at higher wt.% of Sr atoms. These observations are explained by the Burstein-Moss shift and the renormalization process respectively. The dielectric constant values are found to be increased for the 3 and 5 wt.% of Sr dopants PbI_2 and the observed increases is attributed to the hopping conduction and the space charge region developed at the PbI_2 surface. The outcomes signify that the fabricated Sr:PbI_2 are useful in optoelectronic & PV applications.

Acknowledgement

This research was funded by the Deanship of Scientific Research at Princess Nourah bint Abdulrahman University through the Fast-track Research Funding Program.

Declaration of conflict of interest

Authors have no conflict to declare in this work

References

1. Cui, J. Zinc oxide nanowires. *Mater. Charact.*, 2012, 64, 43–52.

2. Kandalkar, S. G.; Dhawale, D. S.; Kim, C. K.; Lokhande, C. D. Chemical synthesis of cobalt oxide thin film electrode for supercapacitor application. *Synth. Met.*, 2010, 160, 1299–1302.

3. Lee, C. T.; Chen, H. W.; Lee, H. Y. Metal-oxide-semiconductor devices using Ga_2O_3 dielectrics on n-type GaN. *Appl. Phys. Lett.*, 2003, 82, 4304–4306.

4. Lokhande, C. D.; Dubal, D. P.; Joo, O. S. Metal oxide thin film based supercapacitors. *Curr. Appl. Phys.*, 2011, 11, 255–270.

5. So, H.; Park, W. Attachable freezing-delayed surfaces for ultraviolet sensing using GaN photodetector at low temperature in air. *Appl. Surf. Sci.*, 2019, 473, 261–265.

6. Zhang, B.; Liu, Y. A review of GaN-based optoelectronic devices on silicon substrate. *Chinese Sci. Bull.*, 2014, 59, 1251–1275.

7. Zhang, L.; Wang, S.; Shao, Y.; Wu, Y.; Sun, C.; Huo, Q.; Zhang, B.; Hu, H.; Hao, X. One-step fabrication of porous GaN crystal membrane and its application in energy storage. *Sci. Rep.*, 2017, 7, 44063.

8. Beckmann, P. A. A review of polytypism in lead iodide. *Cryst. Res. Technol.*, 2010, 45, 455–460.

9. Goto, T.; Tanaka, H.; Exciton study in PbI_2 microcrystallites by pump-probe method. *Solid State Commun.*, 1994, 89, 17–21.

10. Goto, T.; Saito, S.; Tanaka, H. Size quantization of excitons in PbI_2 microcrystallites. *Solid State Commun.*, 1991, 80, 331–334.

11. Tanaka, K.; Hosoya, T.; Fukaya, R.; Takeda, J. A new luminescence due to an exciton-exciton collision process in lead iodide induced by two-photon absorption. *J. Lumin.*, 2007, 122(123), 421–423.

12. Ando, M.; Yazaki, M.; Katayama, I.; Ichida, H.; Wakaiki, S.; Kanematsu, Y.; Takeda. J. Photoluminescence dynamics due to biexcitons and exciton-exciton scattering in the layered-type semiconductor PbI_2. *Phys. Rev. B.*, 2012, 86, 155206.

13. Yang, Y.; Ostrowski, D. P.; France, R. M.; Zhu, K.; van de Lagemaat, J.; Luther, J. M.; Beard, M. C. Observation of a hot-phonon bottleneck in lead-iodide perovskites. *Nat. Photonics.* 2016, 10, 53–59.

14. Gujar, T. P.; Unger, T.; Schönleber, A.; Fried, M.; Panzer, F.; van Smaalen, S.; Köhler, A.; Thelakkat, M. The role of PbI_2 in $CH_3NH_3PbI_3$ perovskite stability, solar cell parameters and device degradation. *Phys. Chem. Chem. Phys.*, 2018, 20, 605–614.

15. Gon, H. B.; Veeraiah, N. Dielectric properties of LiF single crystals. *J. Mater. Sci.*, 1981, 16, 2571–2574.

16. Liu, J.; Liang, Z.; Xu, B.; Xiang, H.; Xia, Y.; Yin, J.; Liu, Z. Synthesis of PbI_2 nanowires for high sensitivity photodetectors. *RSC Adv.*, 2016, 6, 59445–59449.

17. Kaviyarasu, K.; Sajan, D.; Selvakumar, M. S.; Thomas, S. A.; Anand, D. P. A facile hydrothermal route to synthesize novel PbI_2 nanorods. *J. Phys. Chem. Solids*, 2012, 73, 1396–1400.

18. Reza, S.; Bosman, G.; Islam, M. S.; Kamins, T. I.; Sharma, S.; Williams, R. S. Noise in silicon nanowires. *IEEE Trans. Nanotechnol.*, 2006, 5, 523–528.

19. Bid, A.; Bora, A.; Raychaudhuri, A. K. 1/F noise in nanowires. *Nanotechnology*, 2006, 17, 152–156.

20. Shoji, T.; Hitomi, K.; Tiba, T.; Suehiro, T.; Hiratate. Y. Fabrication of a nuclear radiation detector using the PbI_2 crystal and its response characteristics for gamma-rays. *IEEE Trans.*

Nucl. Sci., 1998, 45, 581–584.

21. Liu, J.; Zhang, Y. Growth of lead iodide single crystals used for nuclear radiation detection of Gamma-rays. *Cryst. Res. Technol.*, 2017, 52, 1600370.

22. Sivalingam, M. M.; Balasubramanian, K. Influence of the concentration of reducing agent on gold nanoparticles decorated reduced graphene oxide and its ammonia sensing performance. *Appl. Phys. A*, 2017, 123, 281.

23. Sivalingam, M. M.; Balasubramanian, K. Morphological tuned preparation of zinc oxide: reduced graphene oxide composites for non-enzymatic fluorescence glucose sensing and enhanced photocatalysis. *Appl. Phys. A,* 2016, 122, 294.

24. Shkir, M.; Yahia, I. S.; Ganesh, V.; Bitla, Y.; Ashraf, I. M.; Kaushik, A.; Alfaify, S. A facile synthesis of Au- nanoparticles decorated PbI_2 single crystalline nanosheets for optoelectronic device applications. *Sci. Rep.*, 2018, 8, 13806.

25. Shkir, M.; Alfaify, S. Tailoring the structural, morphological, optical and dielectric properties of lead iodide through Nd^{3+} doping. *Sci. Rep.*, 2017, 7, 16091.

26. Prabhu, D,; Narayanasamy, A.; Shinoda, K.; Jeyadeven, B.; Greneche, J-M.; and Chattopadhyay, K. Grain size effect on the phase transformation temperature of nanostructured $CuFe_2O_4$, *J. Appl. Phys.*, 2011, 109, 013532.

27. Shah, M. A.; Wahab, M. A. Growth rate and symmetry of polytypes in MX_2-compounds. *J. Mater. Sci. Lett.*, 2000, 19, 1813.

28. Li, Y. F.; Yao, B.; Lu, Y. M.; Cong, C. X.; Zhang, Z. Z.; Gai, Y. Q.; Zheng, C. J.; Li, B. H.; Wei, Z. P.; Shen, D. Z.; Fan, X. W.; Xiao, L.; Xu, S. C.; Liu, Y. Characterization of biaxial stress and its effect on optical properties of ZnO thin films. *Appl. Phys. Lett.*, 2007, 91, 021915.

29. Zhang, X.; Ye, J.; Zhu, L.; Zheng, H.; Liu, G.; Liu, X.; Duan, B.; Pan. X.; and Dai, S. High-efficiency perovskite solar cell prepared by a sandwich structure MAI-PbI_2-MAI precursor film. *Nanoscale*, 2017, 9, 4691-4699.

30. Liu, X.; Zhang, Q.; Yip, J. N.; Xiong, Q.; Sum, T. C. Wavelength tunable single nanowire lasers based on surface plasmon polariton enhanced Burstein-Moss effect. *Nano Lett.*, 2013, 13, 5336–5343.

31. Guo, M; Zhang, X. D. Band gap widening and quantum confinement effects of ZnO nanowires by first-principles calculation. *Mater. Sci. Forum.*, 2011, *675-677*, 243–246.

32. Gibbs, Z. M.; LaLonde, A.; Snyder, G. J. Optical band gap and the Burstein-Moss effect in iodine doped PbTe using diffuse reflectance infrared Fourier transform spectroscopy. *New. J. Phys.*, 2013, 15, 075020.

33. Yogamalar, N. R.; Bose, A. C. Burstein-Moss shift and room temperature near-band-edge luminescence in lithium-doped zinc oxide. *Appl. Phys. A.*, 2011, *103*, 33–42.

34. Zhu, C.; Liu, Y.; Xu, J.; Nie, Z.; Li, Y.; Xu, Y.; Zhang, R.; Wang, F. Bandgap renormalization in single-wall carbon nanotubes. *Sci. Rep.*, 2017, *7*, 11221.

35. Zhu, Y.; Mendelsberg, R. J.; Zhu, J.; Han, J.; Anders, A. Dopant-induced band filling and bandgap renormalization in CdO : In films. *J. Phys. D. Appl. Phys.*, 2013, *46*, 195102.

36. Qin, J.; Qiu, G.; Jian, J.; Zhou, H.; Yang, L.; Charnas, A.; Zemlyanov, D.Y.; Xu, C.Y.; Xu, X.; Wu, W.; Wang. H.; Ye. P. D; Controlled growth of a large-size 2D selenium nanosheet and its electronic and optoelectronic applications. *ACS Nano.*, 2017, 11(10), 10222–10229.

37. Qiu, J.; Li, X.; He, W.; Park, S. J.; Kim, H. K.; Hwang, Y. H.; Lee, J. H.; Kim, Y. D. The growth mechanism and optical properties of ultralong ZnO nanorod arrays with a high aspect ratio by a preheating hydrothermal method. *Nanotechnology*, 2009, 20, 155603.

38. Iqbal, J.; Jan, T.; Ronghai, Y.; Naqvi, S.H.; Ahmad, I. Doping induced tailoring in the

morphology, band-gap and ferromagnetic properties of biocompatible ZnO nanowires, nanorods and nanoparticles. *Nano-Micro Lett.*, 2014, 6, 242–251.

39. Yagmurcukardes, M.; Peeters, F. M.; Sahin, H. Electronic and vibrational properties of PbI_2: From bulk to monolayer. *Phys. Rev. B.*, 2018, 98, 085431.

40. Baibarac, M.; Smaranda, I.; Scocioreanu, M.; Mitran, R.A.; Enculescu, M.; Galatanu, M.; Baltog, I. Exciton-phonon interaction in PbI_2 revealed by Raman and photoluminescence studies using excitation light overlapping the fundamental absorption edge. *Mater. Res. Bull.*, 2015, 70, 762–772.

41. Chiu, F. C. A review on conduction mechanisms in dielectric films. *Adv. Mater. Sci. Eng.*, 2014, 2014, 578168.

42. Wang, Y.; Xu, C.; Zhang, J.; Du, X.; Yan, Y. Electronic band structure and magnetic properties of I vacancy and nonmetallic atoms doped single layer PbI_2. *J. Magn. Magn. Mater.*, 2018, 463, 36–43.

43. Cherifi, Y.; Chaouchi, A.; Lorgoilloux, Y.; Rguiti, M.; Kadri, A.; Courtois, C. Electrical, dielectric and photocatalytic properties of Fe-doped ZnO nanomaterials synthesized by sol gel method. *Process. Appl. Ceram.*, 2016, *10*, 125–135.

Research highlights

1) Facile one pot microwave synthesis of Sr@PbI_2 nanosheets was achieved.
2) XRD, Vibrational studies revealed monophasic PbI_2 synthesis at all Sr contents, EDX spectra and SEM e-mapping studies reveals Sr content and its regular dispersal in the final products.
3) SEM study confirms the formation of well-defined nanosheets (NSs) and the optical band gap was varied between 3.26 to 3.29 eV.
4) Dielectric constant and electrical conductivity values are found to be enriched at 3 and 5 wt.% Sr doping.
5) Sr atoms enhance the lifetime of LO phonon by inducing bottleneck effect with enormous charge carriers and such phenomena is very significant for hot carrier solar cell devices.

Declaration of interests

☒ The authors declare that they have no known competing financial interests or personal relationships that could have appeared to influence the work reported in this paper.

☐The authors declare the following financial interests/personal relationships which may be considered as potential competing interests: